ELSEVIER

Turbulence control with wall-adjacent thin layer damping spanwise velocity fluctuations

Shin-ichi Satake and Nobuhide Kasagi
Department of Mechanical Engineering, The University of Tokyo, Tokyo, Japan

Direct numerical simulations (DNSs) have been carried out for fully developed turbulent channel flow and heat transfer with an assumption of a thin layer adjacent to the wall, in which a virtual body force acts to damp the spanwise velocity fluctuations. Fourth-order finite difference computations were made over a relatively small computational volume to repeat simulations under various damping force conditions. It is found that both turbulent friction and heat transfer coefficients are substantially reduced in such manipulated flows. Compared with the pumping power saved, the extra dissipation due to the damping is sufficiently small as long as the damping layer exists close to the wall. In addition, the present control method is most efficient if the damping is imposed on the layer in contact with the wall rather than away from the wall. It is observed that the streamwise elongated streaky structures meander less in the spanwise direction and the coherent vortical structures are attenuated in scale and intensity. Thus, the vortex regeneration as well as the primary turbulence mechanisms, such as the production redistribution of Reynolds stresses played by the vortical structures, should be considerably suppressed by the selective damping of the near-wall spanwise velocity fluctuations.

Keywords: wall turbulence; active control; direct numerical simulation; coherent structures; drag reduction

Introduction

Turbulence control has been one of the central issues in modern scientific, engineering, and environmental research efforts. Its potential benefits can be easily recognized if one thinks about the significance of the artificial manipulation of turbulent drag, noise, heat transfer and chemical reaction, to name a few. Although there is considerable empirical knowledge on how to attenuate or enhance these processes, the underlying mechanisms, in most cases, have not been fully explored. Hence, any attempt at optimizing the turbulence control is likely to be based on empiricism or intuition. The turbulent transport processes are known to be ruled by the so-called quasi-coherent structures (Cantwell 1981; Robinson 1991; Kasagi et al. 1995), but their generation mechanisms, of which knowledge is indispensable for developing rational and efficient control methods, still require further study.

Turbulent friction drag is selected as a control target in this paper. Many intensive investigations have been undertaken focusing on possible drag reducing techniques over the decades. Among them, microgrooved riblets are believed to be a most promising passive device for practical applications. However, the drag reduction mechanism also has not been fully revealed. Suzuki and Kasagi (1994) recently carried out detailed experimental measurement along the riblet surface in a turbulent channel flow using the three-dimensional particle tracking velocimetric (3-D PTV) technique and conjectured two possible drag reduction mechanisms from noticeable reduction of spanwise velocity fluctuations. One plausible mechanism is that the riblets impeded the spanwise fluid motion and, hence, the wall splatting (Moin and Kim 1982; Lee and Hunt 1988); this produces the pressure reflection, which might suppress the wall-layer vortex regeneration (Hamilton et al. 1995) and/or damp the vortex itself. The other is the formation of a virtually free-slip plane at the level of the riblet crests; it may not trigger the regeneration mechanism of the coherent vortices (streamwise vorticity).

The objective of the present work is to study further the former of the above two dynamical effects by making direct numerical simulations (DNSs) of turbulent channel flow. Direct numerical simulation is known to have the ability to guide testing and designing of turbulence control methodologies because of the availability of all flow variables at any spatial location and the ability to alter flow boundary conditions readily (Jung et al. 1992; Choi et al. 1994; Coleman et al. 1995). In the present simulations, we assume that a thin layer exists adjacent to the wall, where a body force acts to impede the spanwise velocity.

Address correspondence to Professor N. Kasagi, Department Mechanical Engineering, University of Tokyo, Hongo 7-3-1, Bunkyo-ku, Tokyo 113, Japan.

Received 26 January 1995; accepted 29 February 1996

Int. J. Heat and Fluid Flow 17: 343–352, 1996

655 Avenue of the Americas, New York, NY 10010

0142-727X/96/$15.00
PII S0142-727X(96)00034-1

This is the consequence of direct similarity to the microgrooved surface, which impedes the spanwise fluid motion. The virtual decelerating body force, whose magnitude is proportional to the spanwise velocity, is introduced into the w-momentum equation. Particular attention is paid to the statistical characteristics of turbulence as well as to the time evolution of the coherent vortical structures. They are compared with the authors' previous DNS results obtained in an ordinary channel and also in a channel where the spanwise velocity component was allowed to slip freely on the wall (this latter case simulated the other of the two dynamic effects mentioned above). The observations of the near-wall turbulence under these different dynamical conditions would offer an additional benefit in that we might better understand the inherent regeneration mechanism of the wall-layer vortices.

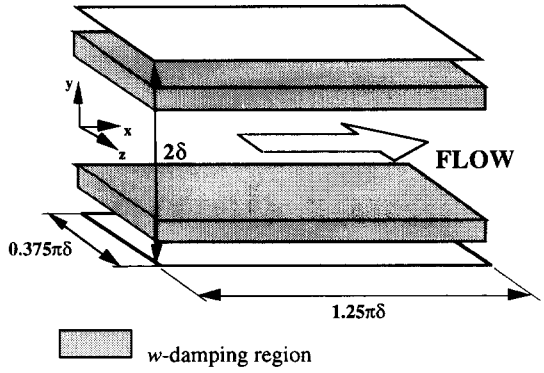

Figure 1 Computational volume and coordinates

Numerical procedure

The convective and viscous terms in the momentum equations were discretized by using the fourth-order central finite difference method proposed by Kajishima (1993) on the staggered grid. The scheme consistent with the continuity equation was adopted for the convective term, while that consistent with the momentum equations was adopted for the budget equations of the Reynolds stress tensor. This scheme has been shown to provide good agreement with the DNS data obtained by the spectral method (Satake and Kasagi, 1994a). For time integration, the second-order Adams–Bashforth scheme was adopted for the nonlinear terms, and the Crank–Nicolson scheme was used for the viscous terms. The time integration was made by the partially implicit fractional step method developed by Kim and Moin (1985). The discretized Poisson equation of pressure was solved by a fast Fourier transform (FFT) in the streamwise and spanwise directions and by TDMA with the fourth-order compact finite difference method of Lele (1992) in the wall-normal direction.

Computational conditions

The flow geometry and the coordinate system are shown in Figure 1. The Reynolds number, which is based on the wall friction velocity u_τ and channel half-width δ, is kept at 150 in all test cases. The computational domain is relatively small and similar to the "minimal flow unit" used by Jiménez and Moin (1991) and Hamilton et al. (1995). It was conjectured that the flow dynamics as well as turbulence structures would be more clearly observed with a reduced degree of inherent radomness. Thus, the streamwise and spanwise computational periods are $1.25\pi\delta$ and $0.375\pi\delta$ (589 and 176 wall units), respectively. Note that only one low-speed streak and just two or three vortical structures are found within the computational domain. Although the turbulence statistics in the region away from the wall can be substantially different from those obtained from computations with a "regular sized" channel (Jiménez & Moin), the turbulence statistics in the near-wall region are very similar to those found in the regular channel. It is, therefore, believed that the key mechanism that maintains turbulence in the minimal flow is nearly the same as that in the regular channel.

The number of grid points is $48 \times 97 \times 36$ in the x-, y-, and z-directions, respectively. A uniform grid with spacings $dx^+ \sim 12.3$ and $dz^+ \sim 4.9$ is used in the x- and z-directions; whereas, a nonuniform mesh of 97 points with a hyperbolic tangent distribution is used in the y-direction. The first mesh point away from the wall is at $y^+ = 0.127$, and the maximum spacing at the channel centerline is 7.63 wall units.

Notation

b_{ij}	stress anisotropy, $b_{ij} = \overline{u_i u_j}/2k - \delta_{ij}/3$
C_f	friction coefficient
c_p	specific heat at constant pressure
h	heat transfer coefficient
II	second anisotropy invariants, $II = -b_{ij}b_{ji}/2$
III	third anisotropy invariants, $III = b_{ij}b_{jk}b_{ki}/3$
k	turbulent kinetic energy
Nu	Nusselt number, $\mathrm{Nu} = 2h\delta/\lambda$
Pr	molecular Prandtl number, $\mathrm{Pr} = \rho c_p \nu/\lambda$
p	pressure
q	heat flux
Re_b	Reynolds number, $\mathrm{Re}_b = 2U_b\delta/\nu$
Re_τ	Reynolds number, $\mathrm{Re}_\tau = u_\tau\delta/\nu$
U	mean velocity
U_b	bulk mean velocity
u, v, w	velocity components in the x, y, and z directions
u_i	velocity component in the ith direction
u_τ	friction velocity, $u_\tau = (\tau_w/\rho)^{1/2}$
x, y, z	streamwise, wall-normal, and spanwise coordinates
x_i	Cartesian coordinates

Greek

α	damping parameter
δ	channel half-width
η	ratio of the pumping power saved to the damping dissipation, Equation 5
Θ	bulk mean temperature
θ	temperature
θ_τ	friction temperature, $\theta_\tau = q_w/\rho c_p u_\tau$
λ	thermal conductivity
ν	kinematic viscosity
ρ	density
τ_w	wall shear stress
ϕ_{ij}	pressure–strain correlation tensor
ω_x	vorticity component in the x-direction

Subscript

$(\,)_{\mathrm{rms}}$	root-mean-square value
$(\,)'$	fluctuating component
$(\,)^+$	normalized by the wall variables
$\overline{(\,)}$	ensemble average over the x–z plane and time

The no-slip boundary condition was imposed on the two walls, and the spanwise velocity was damped in the vicinity of both walls, as shown in Figure 1. Air was chosen as the test fluid, and the Prandtl number Pr was 0.71. Any buoyancy effect was neglected, hence the temperature was considered as a passive scalar. On the two walls, a uniform heat flux boundary condition was imposed. Further details of the thermal boundary condition can be found in Kasagi et al. (1992).

An externally imposed body force term is introduced to the w-momentum equation, which is given as:

$$\frac{\partial w}{\partial t}+u\frac{\partial w}{\partial x}+v\frac{\partial w}{\partial y}+w\frac{\partial w}{\partial z}$$

$$=-\frac{\partial p}{\partial z}+\frac{1}{\mathrm{Re}_\tau}\left(\frac{\partial^2 w}{\partial x^2}+\frac{\partial^2 w}{\partial y^2}+\frac{\partial^2 w}{\partial z^2}\right)-\alpha w, \qquad (1)$$

where the velocities are nondimensionalized by u_τ. The last term on the right-hand side of Equation 1 is the virtual body force term, whose strength is given by a dimensionless constant α, (>0). Nonzero values of α are assumed in the prescribed layer parallel to the wall, as shown in Table 1. In Cases 1A ~ 1C, α is gradually increased up to 4; whereas, in Cases 2A ~ 2D the damping layer of thickness $\Delta y^+ = 10$ is shifted away from the wall.

The initial velocity field was generated from the instantaneous velocity field of the DNS of Kasagi et al. (1992). The governing equations were integrated forward in time until the numerical solutions reached a statistically steady state, and then the computation was further continued for about $2880\nu/u_\tau^2$ in order to calculate turbulence statistics as ensemble averages over space and time. Note that our previous DNS (Case WS, Satake and Kasagi 1994b) with the free-slip condition for the spanwise velocity component on the wall was carried out by the same numerical method. All the results discussed in the following section are nondimensionalized by the wall friction velocity u_τ and the kinematic viscosity ν.

Results and discussion

The mean flow parameters and the skin friction coefficients obtained are summarized in Table 1, where Re_m, C_f, and C_{f0} denote the bulk-mean Reynolds number based on δ and U_m and two skin friction coefficients, respectively. The skin friction coefficient C_{f0} for the ordinary case ($\alpha = 0$) has a slight deviation from the empirical formula of Dean (1978), as shown in Figure 2, so that C_{f0} in Table 1 has been estimated by fitting the following equation,

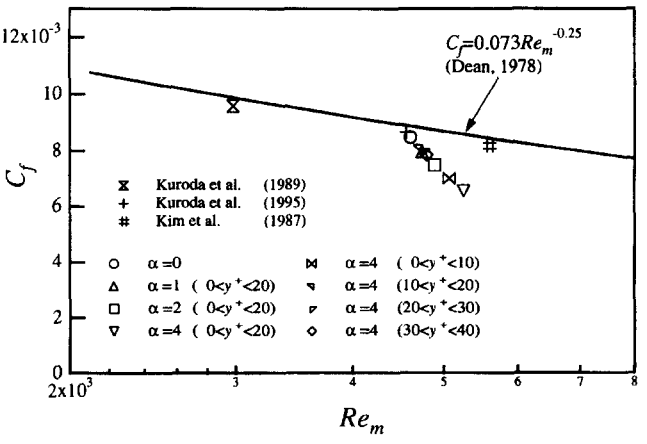

Figure 2 Dependence of skin-friction coefficient on Reynolds number

$$C_{f0} = 0.0698\mathrm{Re}_m^{-0.25} \qquad (2)$$

which has the same dependence on Re_m as the original formula. The Nusselt number obtained in each corresponding case is shown in Table 2. The Nusselt number Nu_0 for $\alpha = 0$ been calculated from the following modified equation:

$$\mathrm{Nu}_0 = 0.0206\mathrm{Re}_m^{0.8}\mathrm{Pr}^{0.4} \qquad (3)$$

which is derived from the empirical formula of Kays and Crawford (1980). In all cases with $\alpha \neq 0$, both friction and heat coefficients are decreased. Note that the bulk Reynolds number is increased in drag-reducing cases, because the streamwise mean pressure gradient is kept constant in the present simulations.

Table 2 Nusselt numbers

Case	α	$\mathrm{Nu} = 2h\delta/\lambda$	$\mathrm{Nu}/\mathrm{Nu}_0$
0	$\alpha = 0$	15.4	1
1A	$\alpha = 1$ ($y^+ = 0 \sim 20$)	14.8	0.926
1B	$\alpha = 2$ ($y^+ = 0 \sim 20$)	14.5	0.885
1C	$\alpha = 4$ ($y^+ = 0 \sim 20$)	13.4	0.773
2A	$\alpha = 4$ ($y^+ = 0 \sim 10$)	14.1	0.836
2B	$\alpha = 4$ ($y^+ = 10 \sim 20$)	15.2	0.956
2C	$\alpha = 4$ ($y^+ = 20 \sim 30$)	14.9	0.930
2D	$\alpha = 4$ ($y^+ = 30 \sim 40$)	14.9	0.925
WS	w free-slip	19.4	1.534

Table 1 Skin friction coefficients and bulk-mean Reynolds numbers

Case	α	$\mathrm{Re}_m = 2u_m\delta/\nu$	C_f	C_f/C_{f0}
0	$\alpha = 0$	4605	8.48×10^{-3}	1
1A	$\alpha = 1$ ($y^+ = 0 \sim 20$)	4740	7.96×10^{-3}	0.945
1B	$\alpha = 2$ ($y^+ = 0 \sim 20$)	4890	7.49×10^{-3}	0.896
1C	$\alpha = 4$ ($y^+ = 0 \sim 20$)	5250	6.55×10^{-3}	0.798
2A	$\alpha = 4$ ($y^+ = 0 \sim 10$)	5070	7.01×10^{-3}	0.847
2B	$\alpha = 4$ ($y^+ = 10 \sim 20$)	4710	8.11×10^{-3}	0.962
2C	$\alpha = 4$ ($y^+ = 20 \sim 30$)	4755	7.96×10^{-3}	0.946
2D	$\alpha = 4$ ($y^+ = 30 \sim 40$)	4791	7.86×10^{-3}	0.936
WS	w free-slip	3540	1.43×10^{-2}	1.58

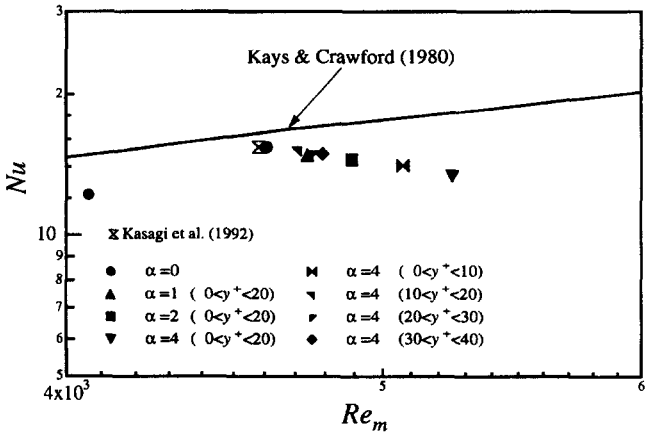

Figure 3 Dependence of Nusselt number on Reynolds number

The effects of the strength parameter and the damping layer location are shown in Figures 4a and 4b, respectively. The drag reduction simply increases with α, and the largest drag reduction, of which ratio C_f/C_{f0} drops to about 80%, is obtained in Case 1C with $\alpha = 4$ over the interval $0 < y^+ < 20$, as shown in Figure 4a. The second largest reduction to about 85% is obtained for Case 2A, where the damping is applied over $0 < y^+ < 10$, in Figure 4b; this thinner damping layer seems almost equally effective, and it is found more effective than that applied to the regions away from the wall in Cases 2B ~ 2D. The ratio of Nu/Nu_0, also plotted in Figures 4a and 4b, is always slightly smaller than that of ratio C_f/C_{f0}.

The near-wall velocity and tempeature profiles for four different values of α are shown in Figure 5, where the results in Case WS are also included. It is evident that the logarithmic profile shifts upward, and its slope becomes steeper as α is increased both in Figures 5a and 5b. Note that the skin friction is increased by more than 50% in Case WS; one thus concludes that the absence of streamwise vorticity at the wall would not lead to turbulent drag reduction. This result supports similar findings by Choi et al. (1994) and Jiménez (1994) on the effect of the free-slip transverse condition at the wall. A similar change in the

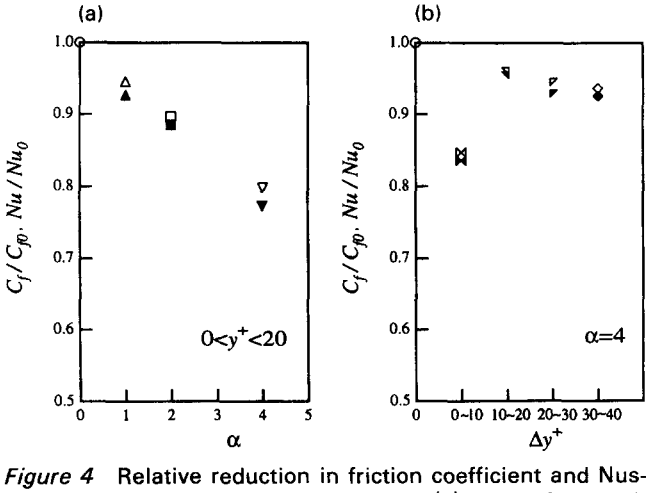

Figure 4 Relative reduction in friction coefficient and Nusselt number: keys as in Figures 2 and 3: (a) effect of strength parameter α; (b) effect of the location of damping layer

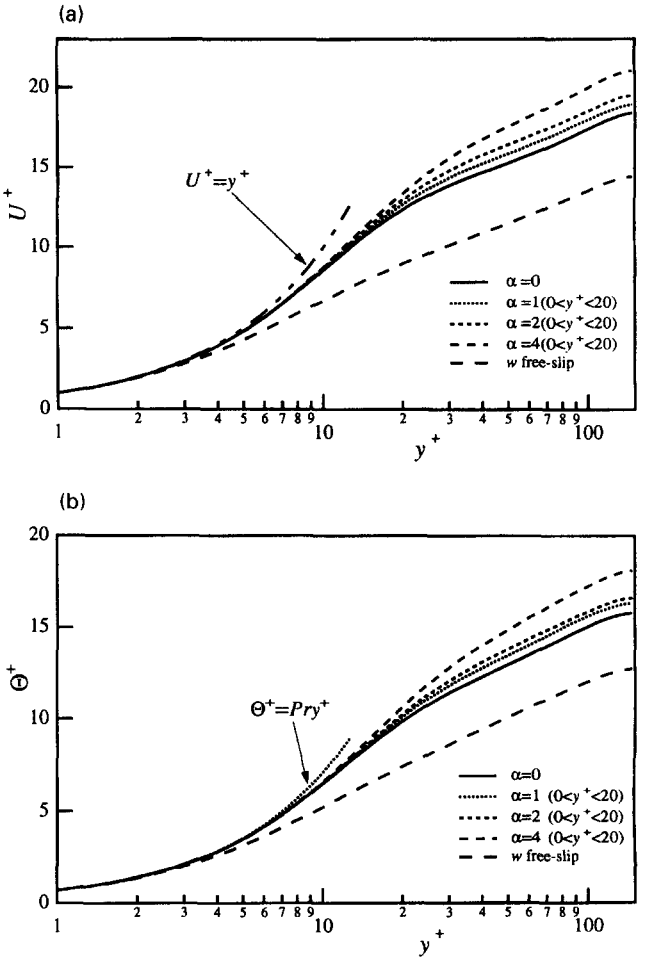

Figure 5 Near-wall mean velocity and temperature profiles: (a) velocity; (b) temperature

logarithmic profile has been reported previously in the drag-reducing flows on riblets by Choi et al. (1993) and Suzuki and Kasagi (1994), and in the turbulence control simulation by Jung et al. (1992) and Choi et al. (1994).

Figure 6 shows the mean velocity and temperature profiles for various locations of the damping layer (of $\Delta y^+ = 10$ in thickness). Every profile for $\alpha = 4$ deviates above that for $\alpha = 0$. In accordance with the relative change in the skin friction coefficient, the deviation is largest when the damping is imposed on the layer attached to the wall; whereas, the damping in the layer farthest from the wall gives the second largest deviation. It is of interest that the turbulent flow field is most affected by the local w-damping when it is imposed beneath or above, but not *in* the buffer layer where the turbulent production rate is maximum. Coleman et al. (1995) studied nonequilibrium three-dimensional (3-D) turbulent boundary layers, and obtained a similar result, namely that application of a spanwise shear led to reduction of both the turbulent kinetic energy and Reynolds stress with the largest reduction occurring when the shear was applied between $y^+ = 0$ and 10. The temperature profiles in Figure 6b for $\alpha \neq 0$ change in a similar way to the velocity profiles, but somewhat less strongly; this is because the present Prandtl number is close to 1.

The total and Reynolds shear stresses are shown in Figure 7. The fact that the total stress distributes linearly gives us confi-

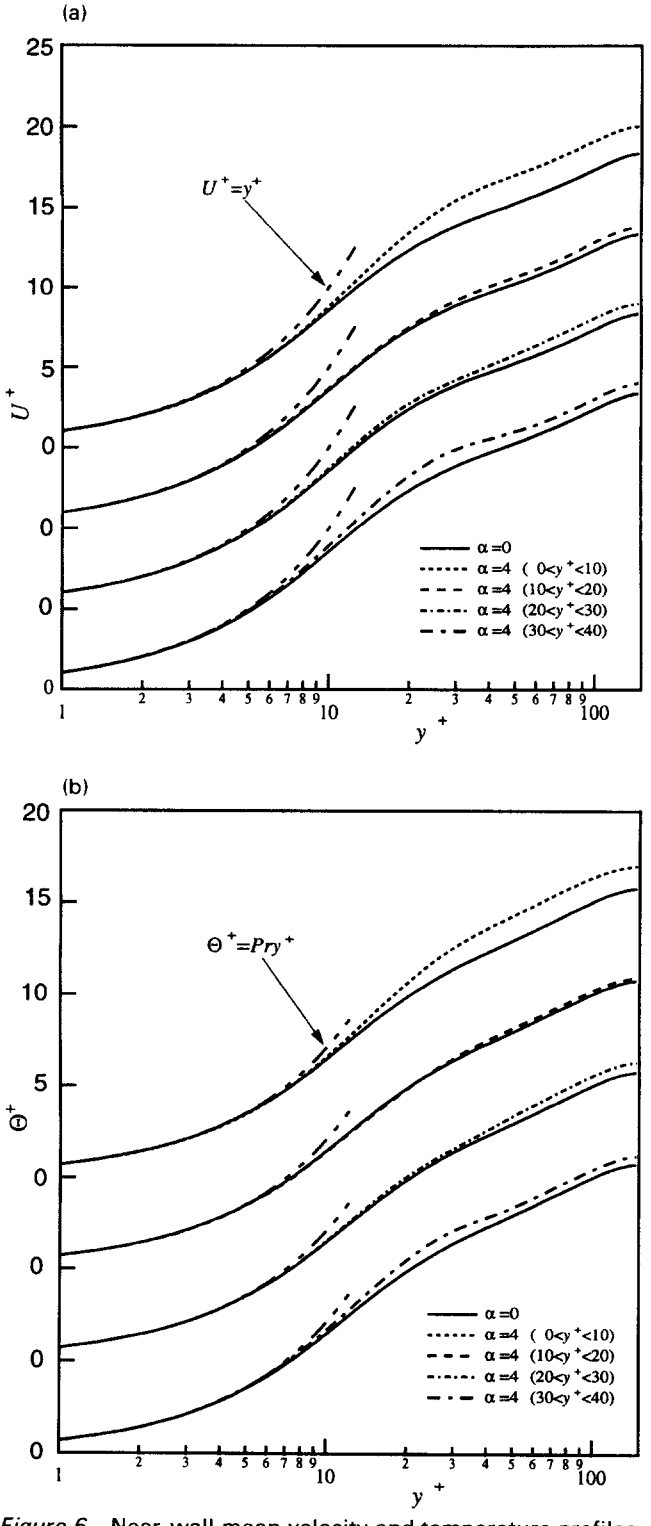

Figure 6 Near-wall mean velocity and temperature profiles; (a) velocity; (b) temperature

dence that the present statistics have been sufficiently sampled after the statistically stationary state was reached. It is evident that the near-wall Reynolds shear stress is reduced considerably by the presence of the w-damping layer, and the maximum Reynolds stress moves away from the wall.

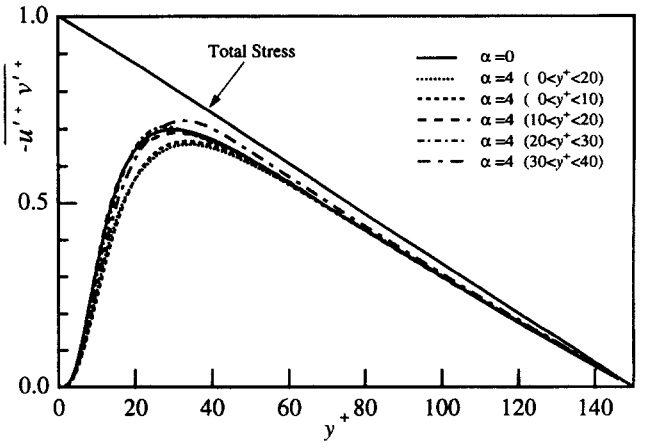

Figure 7 Reynolds shear stress

The root-mean-square (rms) velocity and temperature fluctuations are shown in Figures 8 and 9. In general, the streamwise component becomes larger with w-damping, but the increase is least when the damping is applied at $0 < y^+ < 10$. As the damping layer is moved toward the channel center, the location of maximum u'_{rms} moves slightly away from the wall. In Figure 8(b), the value of v'_{rms} near the wall decreases in all cases with the w-damping. It is natural that the damping effect is especially strong in the w'_{rms} distribution, where a concavity appears at the location of the damping layer because of the direct suppressive effect there. The magnitude of the w-damping effect is largest when the damping is applied at $30 < y^+ < 40$. Choi et al. (1993), however, reported that all turbulent velocity components in the channel manipulated with local blowing and suction become smaller than those in the unmanipulated channel. In Figure 9, it is evident that, as in the streamwise velocity fluctuation, the temperature fluctuation is increased from the location of maximum θ'_{rms} toward the channel center.

The above-mentioned peculiar behavior of the rms velocity fluctuations can be more clearly examined in terms of the invariants of the stress anisotropy tensor, which is defined as $b_{ij} = \overline{u_i u_j}/2k - \delta_{ij}/3$. Figures 10a and 10b represent the second ($-II$) and third (III) invariants, respectively. The second invariant of $-II$ is zero if turbulence is isotropic, while it takes the largest possible value of $1/3$ when turbulence has only one nonzero component (Lumley and Newman 1977). In Figure 10a, II generally takes larger values near the wall owing to the stronger anisotropy there. When the damping layer is introduced near the wall, it affects the anisotropy not only near the wall, but also over a wide region in the channel. The third invariant of III in Figure 10b is an index of whether a component is larger or smaller than the other two. It takes the smallest value of $-1/108$ when a component is zero, and the two other components are equal, while it becomes the largest of $2/27$ when two components are zero. The change in III is similar to that in II, but it is evident that III shows more prominent increase near the wall in the cases the drag reduction is large.

Figure 11 shows the pressure–strain correlations, which stand for the redistribution (or intercomponent transfer) of turbulent kinetic energy. In a two-dimensional (2-D) wall flow, the production due to the shear only exists in the streamwise component, so the two other components gain energy through this redistribution process. As expected, ϕ_{11} is negative, while ϕ_{22} and ϕ_{33} are

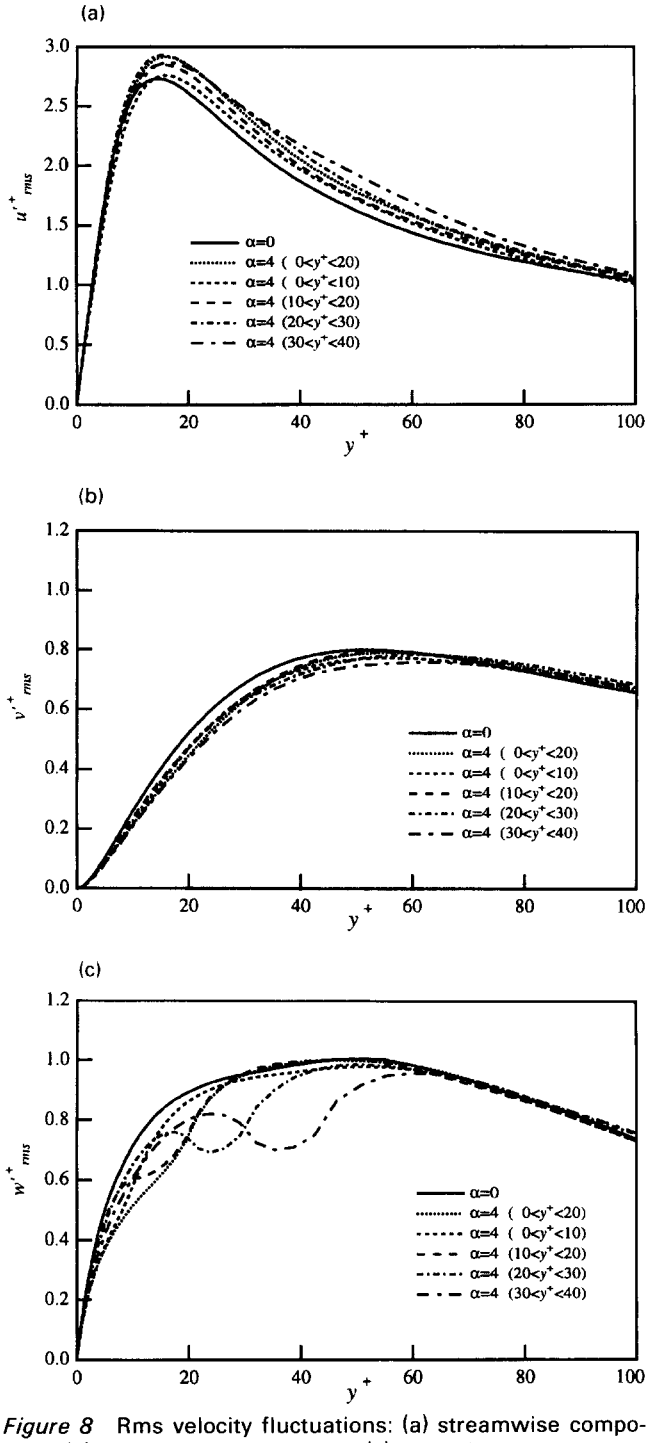

Figure 8 Rms velocity fluctuations: (a) streamwise component; (b) wall-normal component; (c) spanwise component

positive, except for the region close to the wall, where ϕ_{22} is largely positive owing to the wall-blocking effect. When the damping force is imposed, the magnitude of all pressure–strain correlations is decreased considerably near the wall ($y^+ < 10$). This fact is consistent with the enhanced anisotropy of the Reynolds-stress tensor. In contrast, the redistribution is somewhat activated in the region away from the wall. This apparently inconsistent trend can be accounted for by the enhanced turbulent diffusion of $\overline{u'^2}$, which is implied in the energy budget shown later.

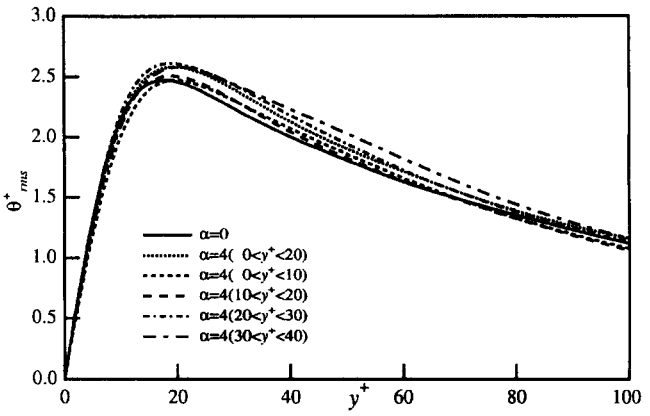

Figure 9 Temperature fluctuations

In Figure 12, it is seen that the rms streamwise vorticity fluctuation is generally decreased with the w-damping layer. The damping at $0 < y^+ < 10$ is most effective in the vicinity of the wall ($y^+ < 15$), while that at $30 < y^+ < 40$ gives the largest decrease in $\omega'_{x\,\mathrm{rms}}$ over a broad region away from the wall. It is of great interest that, even if the damping layer thickness is increased from $0 < y^+ < 10$ to $0 < y^+ < 20$, ω_x does not decrease; indeed it increases in the near-wall region ($y^+ < 25$).

The transport equation of the turbulent kinetic energy is written as:

$$\frac{Dk}{Dt} = \underbrace{-\overline{u'v'}\frac{\partial U}{\partial y}}_{\text{Production}} \underbrace{-\frac{1}{2}\frac{\partial \overline{u'_i u'_i v'}}{\partial y}}_{\text{Turbulent diffusion}} + \underbrace{\nu\frac{\partial^2 k}{\partial y^2}}_{\text{Viscous diffusion}} \underbrace{-\frac{\partial \overline{v'p'}}{\partial y}}_{\text{Pressure diffusion}} \underbrace{-\nu\overline{\frac{\partial u'_i}{\partial x_j}\frac{\partial u'_i}{\partial x_j}}}_{\text{Dissipation}} - \underbrace{\alpha\overline{w'w'}}_{\text{Damping dissipation}} \tag{4}$$

Each term in the above equation near the wall is shown in Figures 13a (Case 2A) and 13b (Case 2D). In Case 2A, the production and dissipation terms decrease at $y^+ < 15$ compared with those of $\alpha = 0$; whereas, they increase in the region further away from the wall. This is due to the reduced Reynolds shear stress near the wall (Figure 7) and the increased mean velocity gradient in the logarithmic region (Figure 6). Note that the same tendency can be observed in the results of Choi et al. (1993). The damping dissipation term is found to be generally small, although it is appreciable in the $\overline{w'^2}$ budget (not shown here), and it is multiplied by a factor of ten in Figures 13a and 13b. Its distribution appears almost linear in the vicinity of the wall in Case 2A, while almost constant in the logarithmic layer in Case 2D. Naturally, the damping dissipation rate is larger in Case 2D, because the spanwise velocity fluctuation is larger away from the wall. Note that the turbulent diffusion is also appreciably increased at $y^+ > 20$.

The efficiency of the process under study is evaluated by referring to Choi et al. (1994); i.e., by estimating the ratio of the pumping power saved to the damping dissipation rate (or the work required for control):

$$\eta = ((-\mathrm{d}p^+/\mathrm{d}x^+|_u + \mathrm{d}p^+/\mathrm{d}x^+|_\mathrm{d})U_m^+) \Big/ \frac{1}{V}\int_V \alpha\overline{w'^+w'^+}/\mathrm{Re}_\tau\,\mathrm{d}V \tag{5}$$

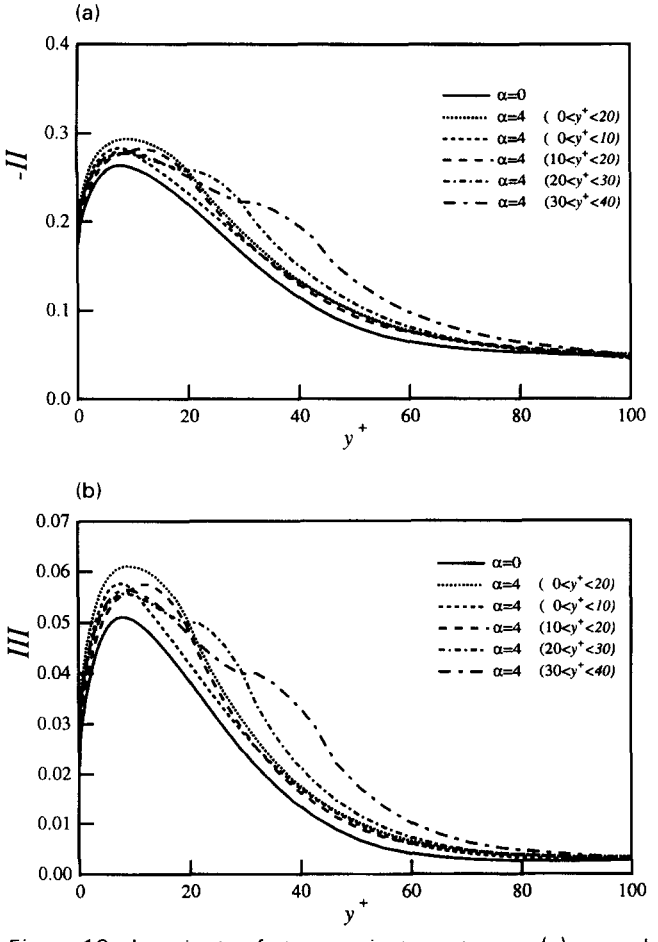

Figure 10 Invariants of stress anisotropy tensor: (a) second invariant; (b) third invariant

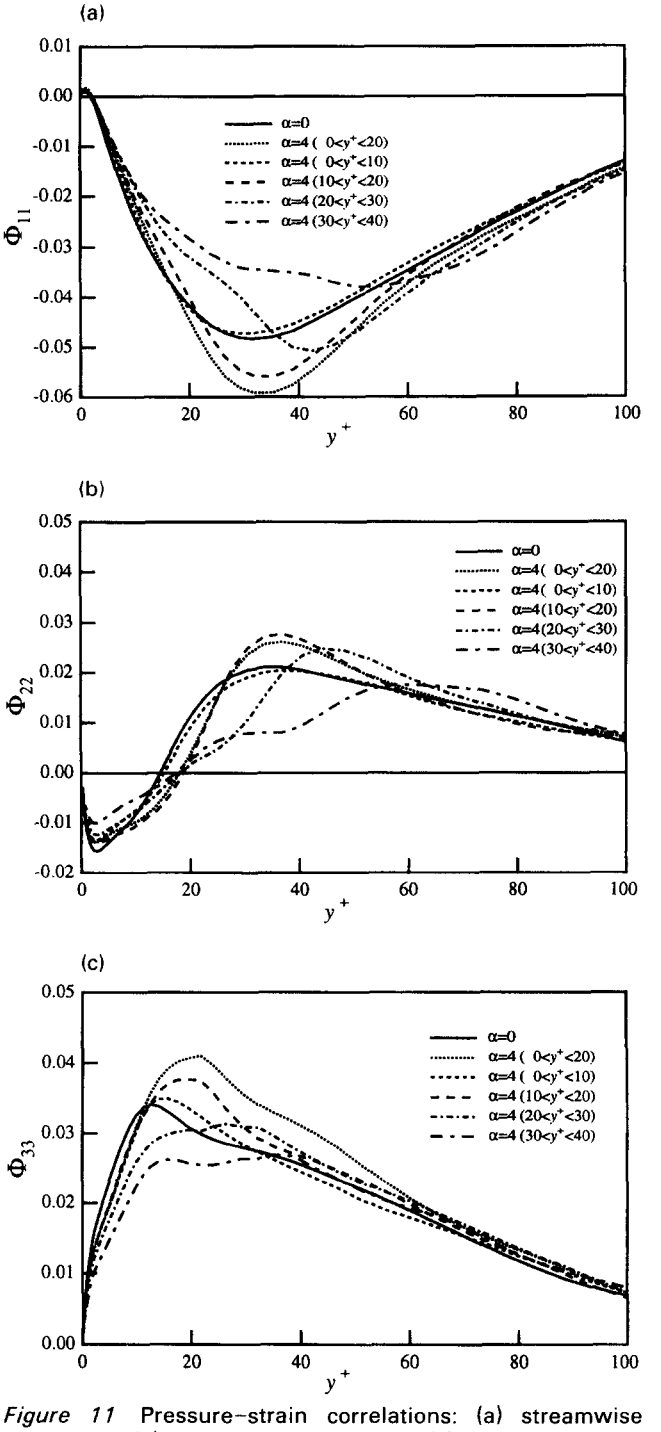

Figure 11 Pressure–strain correlations: (a) streamwise component; (b) wall-normal component; (c) spanwise component

where $-dp^+/dx^+|_u$, and $-dp^+/dx^+|_d$ are the mean pressure gradients in the undamped and w-damped channels, respectively. Because the present simulations were carried out by keeping the mean pressure gradient constant, the baseline pressure gradient at the same bulk Reynolds number cannot be calculated and it is estimated from the modified Dean's formula of Equation 2. The dependence of the efficiency on the strength parameter and damping layer location is represented in Figures 14a and 14b, respectively. When $\alpha = 4$ at $0 < y^+ < 10$ (Case 2A) and $0 < y^+ < 20$ (Cases 1C), the above efficiency becomes about 80 and 30, respectively, indicating that the damping dissipation should be negligible. As mentioned previously, 15.3% and 20.2% drag reduction is obtained respectively in these Cases. It is obvious that the thinner damping layer is even more advantageous from the viewpoint of the first law of thermodynamics. In contrast, when the damping region exists away from the wall, the extra dissipation is no longer negligible; for example, the efficiency remains to be only 8 when the drag reduction is 6.4% with $\alpha = 4$ at $30 < y^+ < 40$. It is noted that, although the damping dissipation is assumed to be a complete loss of energy in the present evaluation, an additional benefit may possibly be brought about by converting it to some effective energy in future implementation.

Figure 15 represents local low-pressure regions visualized in an instantaneous flow field without the w-damping layer. The low-pressure regions in the large scales have been confirmed to correspond to intense rotational fluid motions (quasi-coherent vortices) in the DNS databases of turbulent boundary layer and channel flows by Robinson (1991) and Kasagi et al. (1995). The latter authors found that these vortices are associated even with the diffusion, redistribution, and destruction mechanisms of Reynolds stresses. A typical banana-shaped inclined streamwise vortex, that appears most frequently in the near-wall region, can

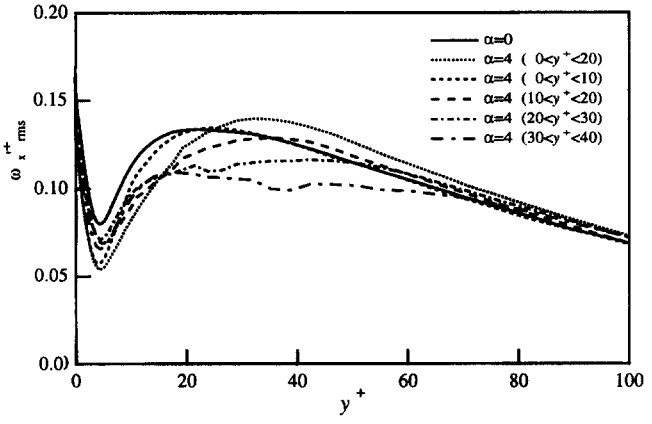

Figure 12 Streamwise vorticity fluctuations

be seen in Figure 15. Because the present simulation uses a small computational volume, the near-wall structures are emphasized enabling them to be very clearly observed.

The time evolution of the flow field in the ordinary ($\alpha = 0$) and w-damped ($\alpha = 4$ at $0 < y^+ < 20$) channels from $t^+ = 0$ to

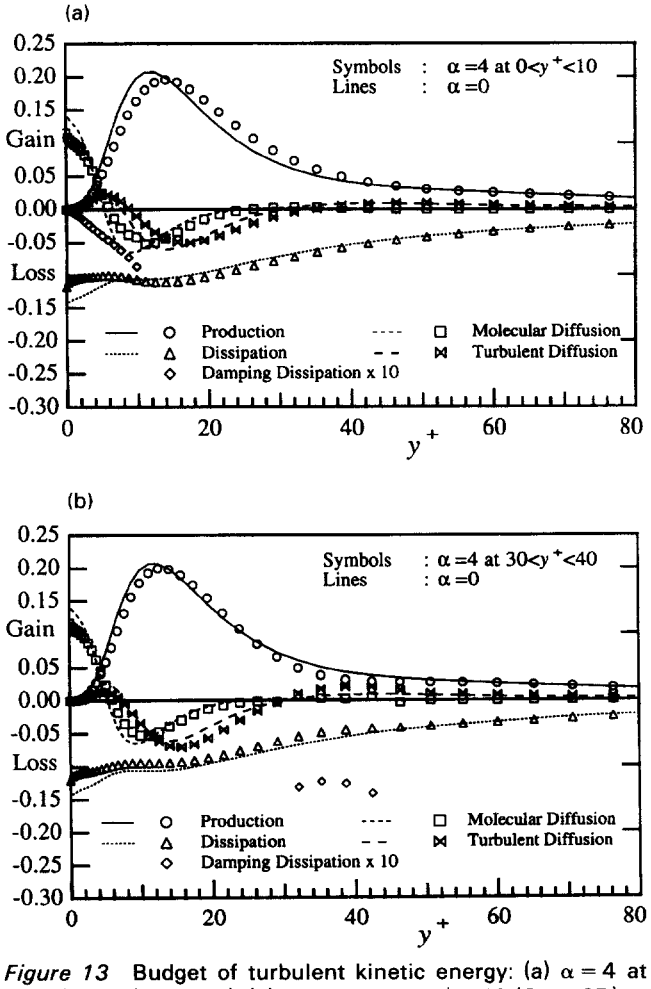

Figure 13 Budget of turbulent kinetic energy: (a) $\alpha = 4$ at $0 < y^+ < 10$ (Case 2A); (b) $\alpha = 4$ at $30 < y^+ < 40$ (Case 2D)

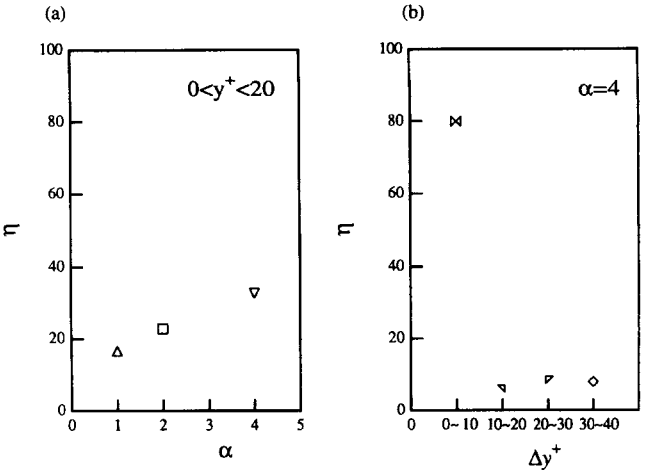

Figure 14 Ratio of pumping power saved to damping dissipation: keys as in Figure 2: (a) effect of strength parameter α; (b) effect of location of damping layer

129.6 is shown in Figure 16a and 16b, respectively. The gray and black contour surfaces in the sequence of top (x–z) views respectively represent the low-pressure and low-speed regions; i.e., vortical structures and wall-layer streaks. The same initial flow field, which has been reached without the w-damping layer, is assumed for both cases at $t^+ = 0$, and then the flow field is observed with and without the w-damping. In the initial period, the structures in the two cases appear almost of the same shape and size, and at the same location; e.g., as can be seen at $t^+ = 57.6$. However, the vortical structures as well as the streaks are drastically altered after $t^+ = 79.2$. The meandering of the streak, which is known to be one of the major phases in the regeneration mechanism of the streamwise vortices (Hamilton et al. 1995), is seen at $t^+ = 57.6$ and later, but this meandering is considerably suppressed in the w-damping channel. Typically at $t^+ = 129.6$ in Figure 16b, the streak is oscillating less in the spanwise direction, and the vortical structure is reduced to a much smaller size; i.e., a weaker vortex. Thus, the flow field becomes markedly quiescent in the w-damped channel. It is believed that the decrease in the streak meandering and the reduced size of vortical structures should lead to the suppression of the vortex regeneration process.

In Figure 17, the low-pressure and high-damping-dissipation regions are visualized at the same instant of $t^+ = 57.6$ in Figure 16b. It is noticed that the regions of large damping dissipation exist beneath most of the vortical structures. Thus, the w-

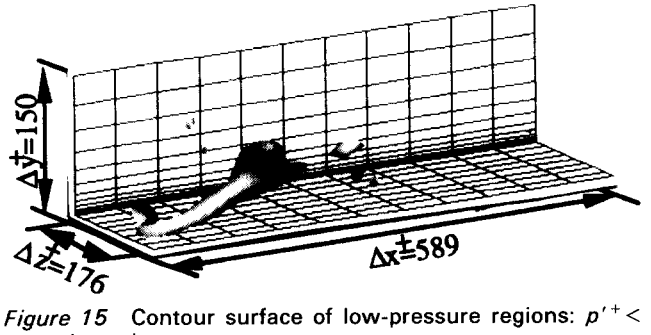

Figure 15 Contour surface of low-pressure regions: $p'^+ < -4.0$ ($\alpha = 0$)

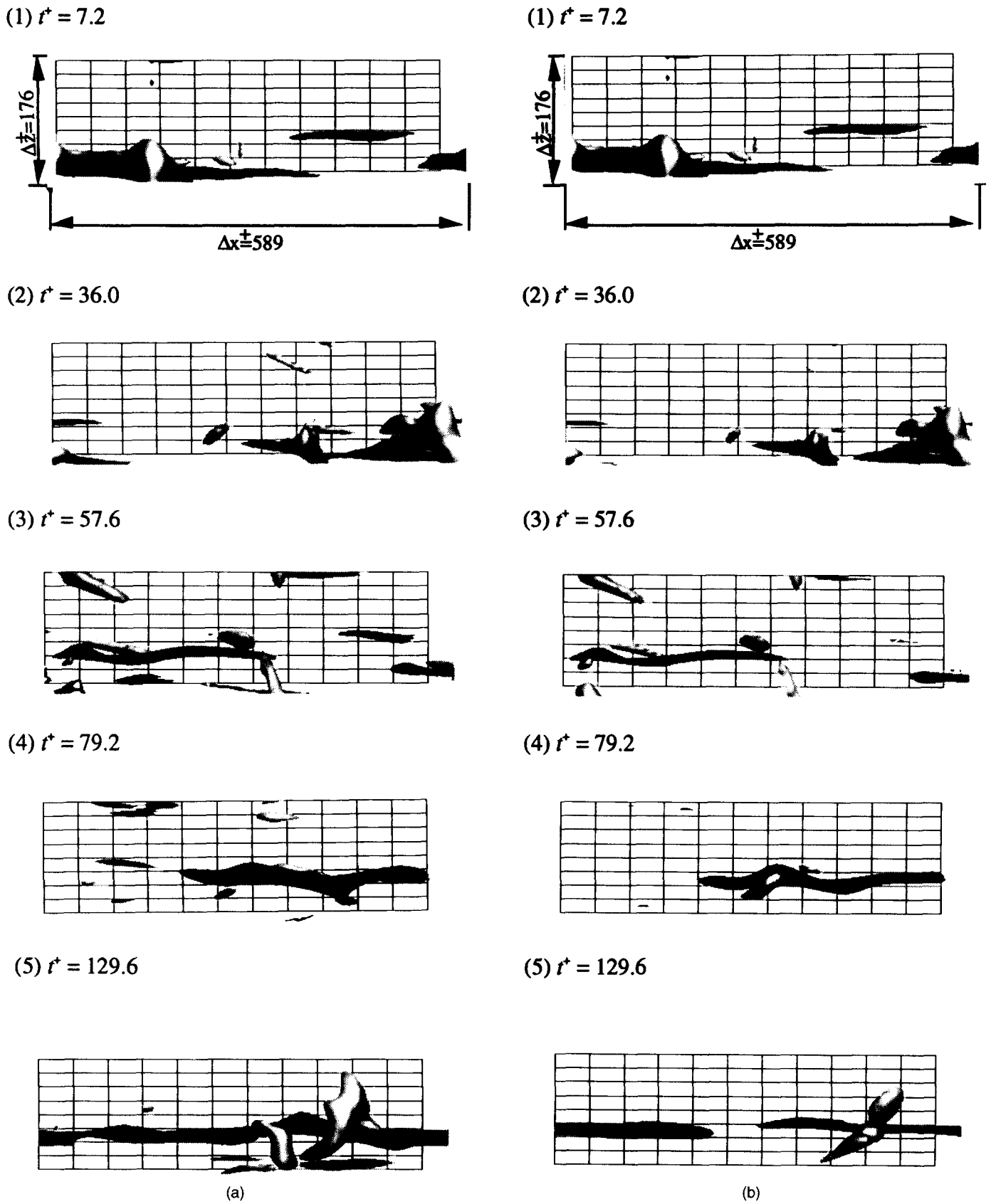

Figure 16 (a) Contour surface of low-pressure and low-speed regions in Case 0 ($\alpha = 0$): gray, $p'^+ < -4.0$; black, $u'^+ < -4.0$; (b) contour surface of low-pressure and low-speed regions in Case 1C ($\alpha = 4$ at $0 < y^+ < 20$): gray, $p'^+ < -4.0$; black, $u'^+ < -4.0$

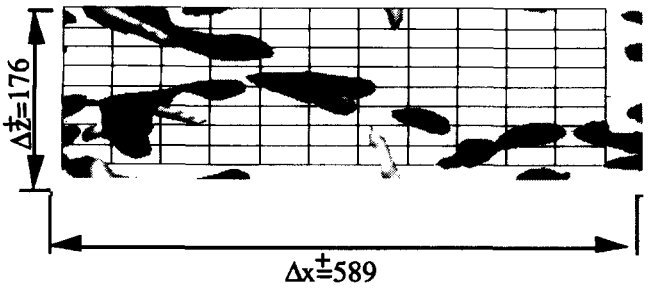

Figure 17 Low-pressure and high-damping-dissipation regions ($t^+ = 57.6$, $\alpha = 4$ at $0 < y^+ < 20$): gray, $p'^+ < -4.0$; black, $-\alpha w'^+ w'^+ / \mathrm{Re}_\tau < -0.035$

damping force effectively decelerates the rotation fluid motion induced by the vortical structures.

Conclusions

A series of direct numerical simulations have been carried out of turbulent channel flow with a thin w-damping layer assumed in the vicinity of the wall. It is found that the w-damping brings about marked reduction in the turbulent friction drag and heat transfer coefficients; e.g., by as much as 20% when $\alpha = 4$ over the range of $0 < y^+ < 20$. The extra dissipation due to the w-damping remains very small as long as the damping layer exists close to the wall, and its magnitude relative to the pumping power saved is only 1/80 when $\alpha = 4$ at $0 < y^+ < 10$. In addition, the present control method is more efficient if the damping force is imposed on the layer in contact with the wall ($0 < y^+ < 10$), rather than on layers away from the wall (say, $30 < y^+ < 40$).

From the observed time evolution of th flow field with the w-damping near-wall layer, it is found that the wall-layer streaks meander less in the spanwise direction. The growth of the coherent vortical structures is attenuated markedly, and this results in the reduced intensity and scale of rotational motion. Thus, the vortex regeneration as well as the important turbulence mechanisms played by the vortical structures, such as the production and redistribution of Reynolds stresses, should be considerably suppressed by the w-damping layer.

Acknowledgments

The authors acknowledge the financial support through the Grant-in-Aids for Scientific Research on Priority Areas (No. 05240103) and for Encouragement of Young Scientists (No. 06003542) by the Ministry of Education, Science, and Culture.

References

Cantwell, B. 1981. Organized motion in turbulent flows. *Annu. Rev. Fluid Mech.*, J. L. Lumley, M. Van Dyke, and H. L. Reed (eds.), **13**, 457–515

Choi, H., Moin, P. and Kim, J. 1993. Direct numerical simulation of turbulent flow over riblets. *J. Fluid Mech.*, **255**, 503–539

Choi, H., Moin, P. and Kim, J. 1994. Active turbulence control for drag reduction in wall-bounded flows. *J. Fluid Mech.*, **262**, 75–110

Coleman, G. N., Kim, J. and Le, A. T. 1995. A numerical study of three-dimensional boundary layers. *Proc. 10th Turbulent Shear Flows*, The Pennsylvania State University, University Park, PA, 29-7-29-12

Dean, R. B. 1978. Reynolds number dependence of skin friction and other bulk flow variables in two-dimensional rectangular duct flow. *J. Fluids Eng.*, **100**, 215–223

Hamilton, J. M., Kim, J. and Waleffe, F. 1995. Regeneration mechanisms of near-wall turbulence structures, *J. Fluid Mech.*, **287**, 317–348

Jiménez, J. 1994. On the structure and control of near wall turbulence. *Phys. Fluids A*, **6**, 944–953

Jiménez, J. and Moin, P. 1991. The minimal flow unit in near-wall turbulence. *J. Fluid Mech.*, **225**, 213–240

Jung, W. J., Mangiavacchi, N. and Akhavan, R. 1992. Suppression of turbulence in wall-bounded flows by high-frequency spanwise oscillations, *Phys. Fluids A*, **4**, 1605–1607

Kajishima, T. 1993. A high-order finite difference method for wall-bounded incompressible flows. *Proc. of the 5th Int. Symposium on Computational Fluid Dynamics, Vol. 1*, Sendai, Japan, 414–419

Kasagi, N., Sumitani, Y., Suzuki, Y. and Iida, O. 1995. Kinematics of the quasi-coherent vortical structure in near-wall turbulence. *Int. J. Heat Fluid Flow*, **16**, 2–10

Kasagi, N., Tomita, Y. and Kuroda, A. 1992. Direct numerical simulation of the passive scalar field in a turbulent channel flow. *J. Heat Transfer*, **114**, 598–606

Kays, W. M. and Crawford, M. E. 1980. *Convective Heat and Mass Transfer*, 2nd ed., McGraw-Hill, New York

Kim, J. and Moin, P. 1985. Application of a fractional-step method to incompressible Navier–Stokes equations. *J. Comp. Phys.*, **59**, 308–323

Kim, J., Moin, P. and Moser, R. 1987. Turbulent statistics in fully developed channel flow at low Reynolds number. *J. Fluid Mech.*, **177**, 133–166

Kuroda, A., Kasagi, N. and Hirata, M. 1989. A direct numerical simulation of the fully developed turbulent channel flow. *Int. Symp. on Computational Fluid Dynamics*, Nagoya, 1174–1179; also Kuroda, A., Kasagi, N. and Hirata, M. 1990. Numerical methods in fluid dynamics, M. Yasuhara et al. (eds.), *J. Soc. Comp. Fluid Dyn.*, **2**, 1012–1017

Kuroda, A., Kasagi, N. and Hirata, M. 1995. Direct numerical simulation of turbulent plane couette-poiseuille flows: Effect of mean shear rate on the near wall turbulent structures. *Turbulent Shear Flows 9* (selected papers from the 9th Int. Symp. on Turbulent Shear Flows), F. Durst, N. Kasagi, B. E. Launder, F. W. Schmidt, K. Suzuki and J. H. Whitelaw (eds.), Springer-Verlag, Berlin, 241–257

Lee, M. J. and Hunt, J. C. R. 1988. The structure of sheared turbulence near a plane boundary. *Proc. CTR Summer Program*, CTR, Stanford University, Stanford, CA, 221–241

Lele, S. K. 1992. Compact finite difference scheme with spectral-like resolution. *J. Comp. Phys.*, **103**, 16–42

Lumley, J. L. and Newman, G. R. 1977. The return to isotropy of homogeneous turbulence, *J. Fluid Mech.*, **82**, 161–178

Moin, P. and Kim, J. 1982. Numerical investigation of turbulent channel flow. *J. Fluid Mech.*, **118**, 341–377

Robinson, S. K. 1991. The kinematics of a turbulent boundary-layer structures. NASA TM-103859

Satake, S. and Kasagi, N. 1994a. Direct numerical simulation of channel flow with collocation grid. *Proc. of the 8th Symposium on Computational Fluid Dynamics*, Tokyo, Japan, 321–324, (in Japanese)

Satake, S. and Kasagi, N. 1994b. DNS of turbulent channel flow with factitiously modified wall boundary condition. *Proc. of the 26th Sump. Turbulence*, Tokyo, Japan, 358–361, (in Japanese)

Suzuki, Y. and Kasagi, N. 1994. Turbulent drag reduction mechanism above a riblet surface. *AIAA J.*, **32**, 1781–1790